Supplementary Information

Nanofibrous Aerogels with Continuous Conductivity Gradient for Ultrabroadband Absorption-Dominant Electromagnetic Interference Shielding

Yaqing Chen[1,2], Huimin He[1], Na Wu[3], Sinan Zheng[4], Xi Liao[5,6*], Jin Zhou[4], Yue Liu[4], Junlin Chen[1], Changxian Wang[7*], Lizhi Xu[1,2,8*], Zhihui Zeng[4*]

[1] Department of Mechanical Engineering, The University of Hong Kong, Hong Kong SAR, China.

[2] Advanced Biomedical Instrumentation Centre Limited, Hong Kong SAR, China.

[3] School of Chemistry and Chemical Engineering, Shandong University, Jinan 250061, China.

[4] State Key Laboratory of Coatings for Advanced Equipment, Key Laboratory for Liquid-Solid Structural Evolution and Processing of Materials, School of Materials Science and Engineering, Shandong University, Jinan 250061, China.

[5] School of Construction Engineering, Shenzhen Polytechnic University, Shenzhen 518055, China.

[6] Department of Architecture, The University of Hong Kong, Hong Kong SAR, China.

[7] Institute of Advanced Structure Technology, Beijing Institute of Technology, Beijing 100081, China.

[8] Materials Innovation Institute for Life Sciences and Energy (MILES), The University of Hong Kong Shenzhen Institute of Research and Innovation (HKU-SIRI), Shenzhen 518057, China.

Corresponding authors. Email: xiliao22@szpu.edu.cn; wangcx@pku.edu.cn; xulizhi@hku.hk; zhihui.zeng@sdu.edu.cn

Supplementary Figures 1-26

Supplementary Tables 1-3

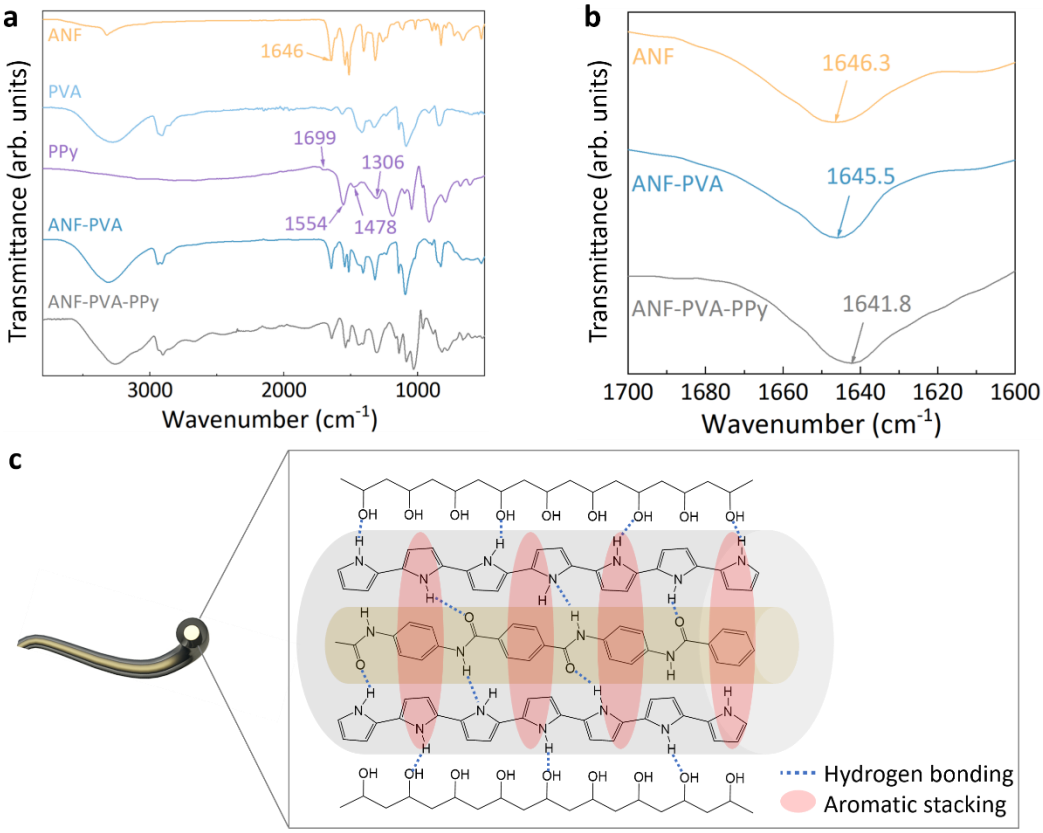

Supplementary Fig. 1 Chemical structures characterized by FTIR and intermolecular interactions of different polymers in MCAs (i.e., ANF-PVA-PPy). a. FTIR transmittance spectra of ANF, PVA, PPy, ANF-PVA, and ANF-PVA-PPy. For polypyrrole, the peaks at 1554 cm^{-1} and 1478 cm^{-1} correspond to the characteristic C=C stretching within the conjugated polymer backbone. Peaks at 1699 cm^{-1} and 1306 cm^{-1} are attributed to the stretching vibrations of C=N and C–N bonds, respectively.[1] For ANF, the peak at 1648 cm^{-1} is contributed by the aramid C=O stretching. The spectral features observed in this study align well with previously reported data, validating the successful synthesis of polypyrrole. b. Enlarged view of the 1700–1600 cm^{-1} region, highlighting the evolution of the aramid C=O stretching.[2] The characteristic peak at 1646.3 cm^{-1} for ANF red shifts slightly to 1645.5 cm^{-1} in ANF-PVA due to hydrogen bonding interactions between ANF and PVA. A more pronounced redshift to 1641.8 cm^{-1} in the ANF-PVA-PPy composite indicates enhanced hydrogen bonding between ANF and PPy. c. Schematic illustration of possible intermolecular interactions within the ANF-PVA-PPy network. π–π stacking and hydrogen bonding are proposed between the aromatic rings and amide groups of PPTA and the PPy chains. Concurrently, PVA forms hydrogen bonds with both PPTA and PPy, facilitating the formation of a physically interconnected hybrid network. FTIR spectra are vertically offset for clarity.

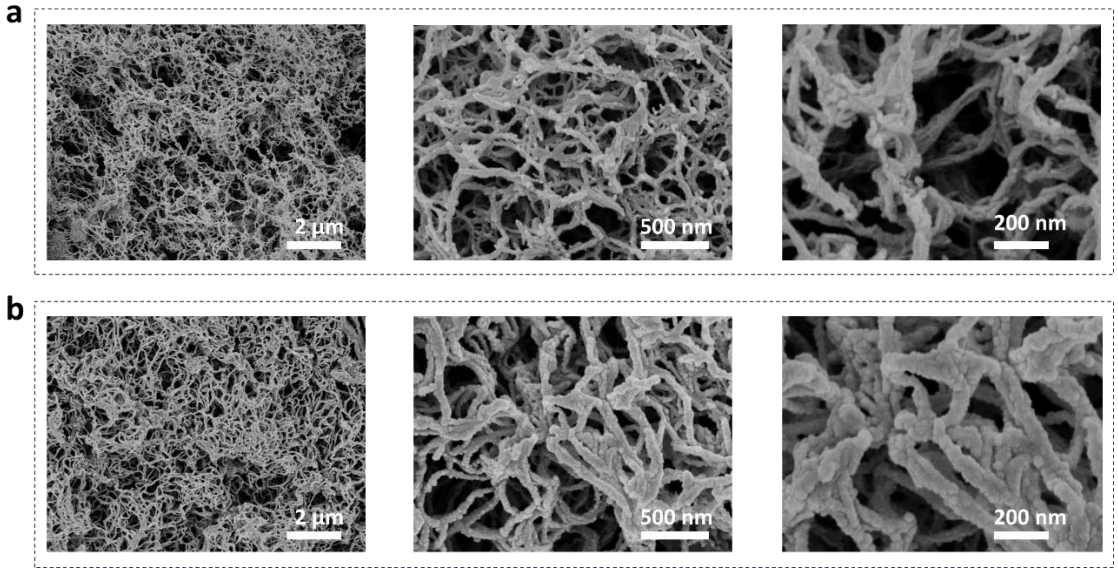

Supplementary Fig. 2 SEM images of ANF-PVA (a) and ANF-PVA-PPy (b) with 94% porosity.

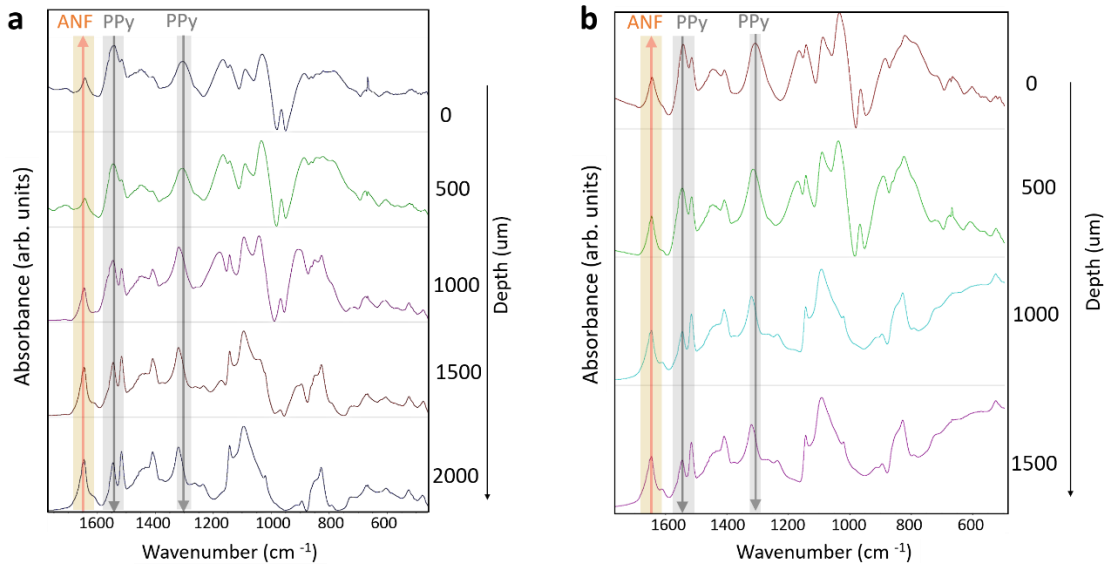

Supplementary Fig. 3 ATR-FTIR absorbance spectra of MCA-88 (a) and MCA-75 (b) samples with downward sliced layers along depth. Both figures exhibit decreasing characteristic peaks for PPy (1554 cm^{-1} for C=C stretching, 1306 cm^{-1} for C-N stretching) and increasing characteristic peaks for ANF (1646 cm^{-1} for C=O stretching). The variation in characteristic peaks is consistent across MCA-88 and MCA-75 samples, indicating a decreasing content of PPy and an increasing content of ANF in the depth direction for MCAs.

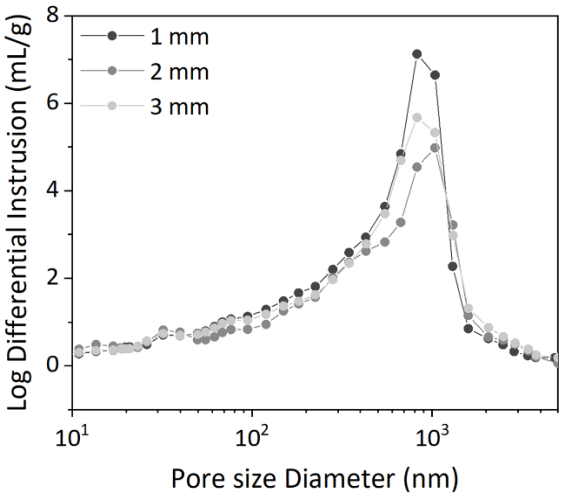

Supplementary Fig. 4 Pore size distribution of ANF-PVA with 94% porosity at various depths of the bulk sample.

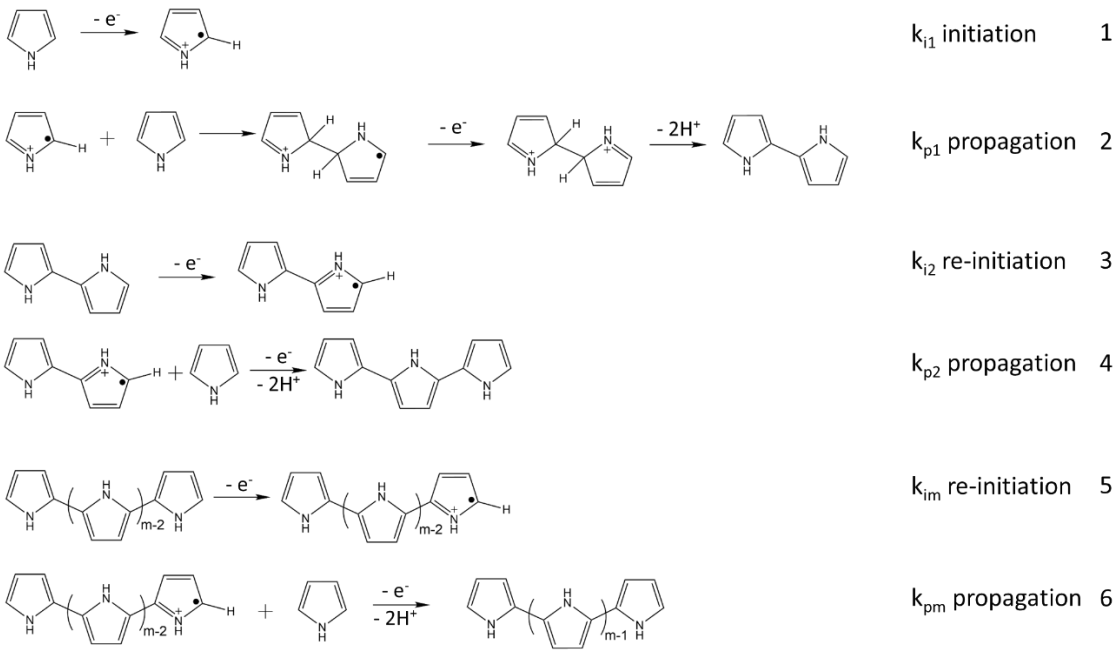

Supplementary Fig. 5 The proposed mechanism of PPy polymerization. The radical cation reacts with a neutral monomer (reaction 1), followed by oxidation and deprotonation to yield a dimer (reaction 2). The dimer is then oxidized immediately, forming a dimeric radical cation (reaction 3), which attacks another monomer, leading to the formation of a trimer (reaction 4). This repeated process results in polymer chain growth and ultimately produces the polymer (reactions 5 and 6).[3]

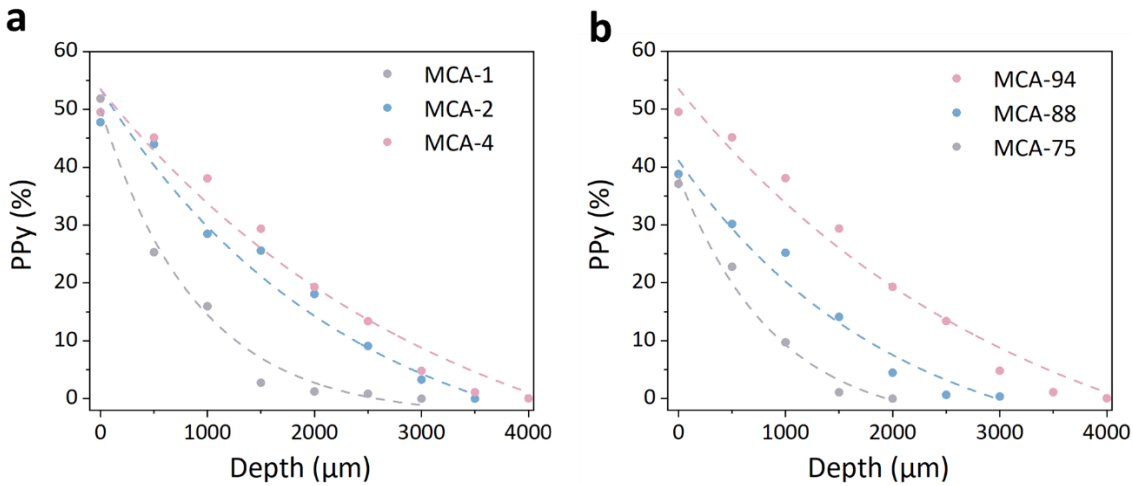

Supplementary Fig. 6 Experimental results of the variation of PPy content in weight percent units. a. The variation of PPy content (represented by PPy weight percent) at different depths of MCA-94 bulk samples with varying diffusion/reaction times. b. The variation of PPy content (represented by PPy weight percent) in MCAs with various porosities when the diffusion/reaction time is 4 h. (Dots represent experimental results; dashed lines indicate fitting curves.)

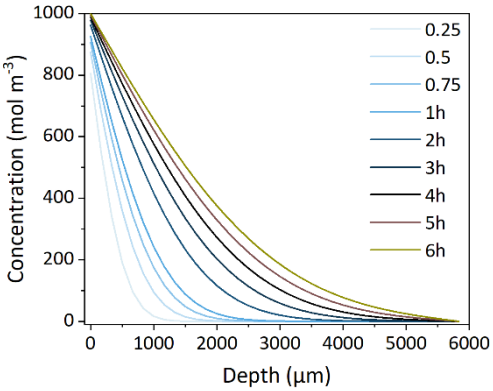

Supplementary Fig. 7 Simulation results of varied gradients of PPy content (represented by pyrrole molar concentration) at different depths of bulk aerogel with varying diffusion/reaction times.

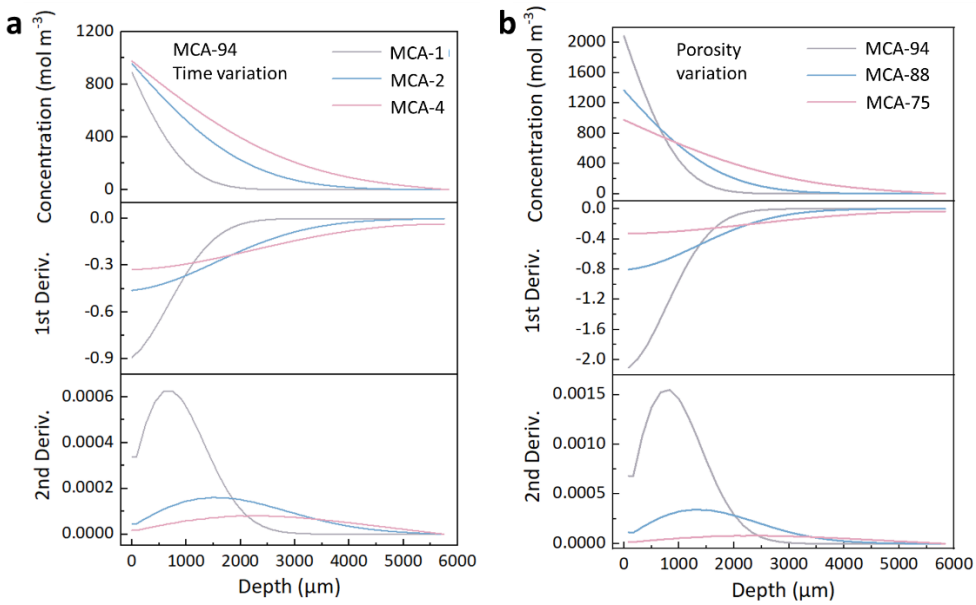

Supplementary Fig. 8 The characteristics of the simulated PPy content gradients (represented by pyrrole molar concentration). a. The concentration gradient, first and second derivatives of the PPy content gradient at downward depth with various diffusion/reaction times of the MCA-94 sample. In the first 1 mm below the top surface, a short reaction time (0.75 h) produces a sharper PPy-content drop, whereas a prolonged reaction time (4 h) yields a smoother concentration profile over the same region, corresponding to a smaller derivative magnitude and weaker curvature. b. The first and second derivatives of the PPy content gradient at a downward depth of MCAs with various porosities when the diffusion/reaction time is 4 h.

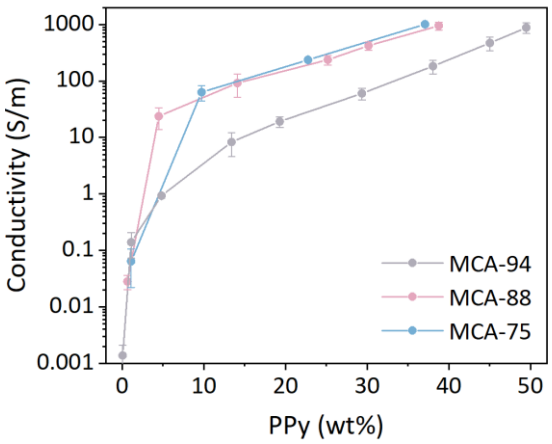

93

94 **Supplementary Fig. 9** Conductivity variation as PPy wt% changes with different
95 porosities. Data are presented as mean ± s.d. from three independent experiments (n=3);
96 error bars represent s.d.

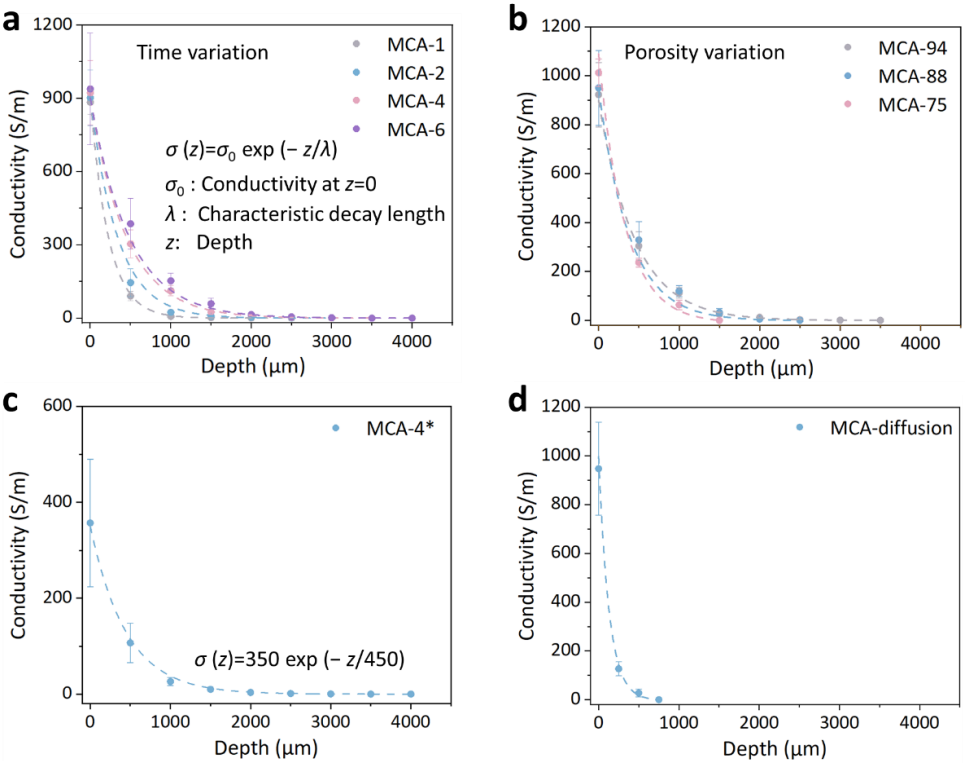

Supplementary Fig. 10 Through-thickness conductivity profiles of different MCAs plotted on a linear y-axis. a. Conductivity profiles versus depth for 94%-porosity of MCAs prepared with various diffusion/reaction times. b. Conductivity profiles versus depth for MCAs of different porosities prepared with a fixed diffusion/reaction time of 4 h. c. Conductivity profile of MCA-4* with reduced surface conductivity prepared in an oxygen-containing atmosphere. d. Conductivity profile of MCA-diffusion prepared by a non-gravity-driven reactant-permeation method and exhibiting a steeper gradient. Symbols represent experimental data and dashed lines are fits to $\sigma(z)=\sigma_0 \exp(-z/\lambda)$, where σ_0 is the surface conductivity at $z = 0$, λ is the characteristic decay length (μm), and z is measured from the high-σ surface toward the low-σ surface. Data points are presented as mean ± s.d. (n = 3 independent samples).

To assess thickness effects, we distinguish the sample thickness from the effective gradient length defined as the PPy-containing gradient region. Unless otherwise noted, the bulk MCAs compared in Fig. 3e–g and Supplementary Table 1 had the same thickness of ~5 mm. Shortening the diffusion/reaction time reduced the conductivity gradient length from ~4.0 to ~2.5 mm and decreased A from 0.84 to 0.76, while lowering the scaffold porosity further confined the gradient length to ~2.0 mm and reduced A to 0.67. In both cases, SE_T remained above 30 dB, indicating that millimeter-scale conductive thickness can provide strong attenuation but does not by itself ensure low reflection. In the present experimentally validated design, 5 mm is the minimum nominal thickness confirmed to satisfy both $R <$ 0.1 and $SE_T >$ 30 dB over 10.2–40 GHz.

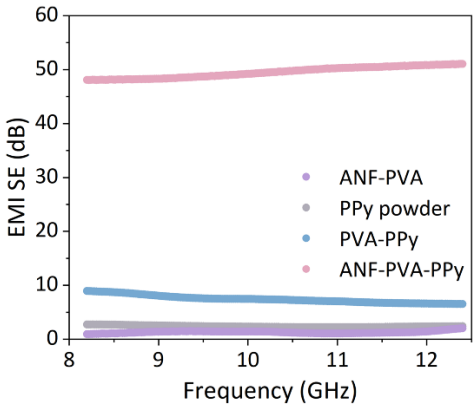

Supplementary Fig. 11 EMI SE of ANF-PVA substrate, PPy powder, PVA-PPy by PPy in situ polymerization in PVA substrate, and ANF-PVA-PPy by PPy in situ polymerization in ANF-PVA substrate with porosity of 94%.

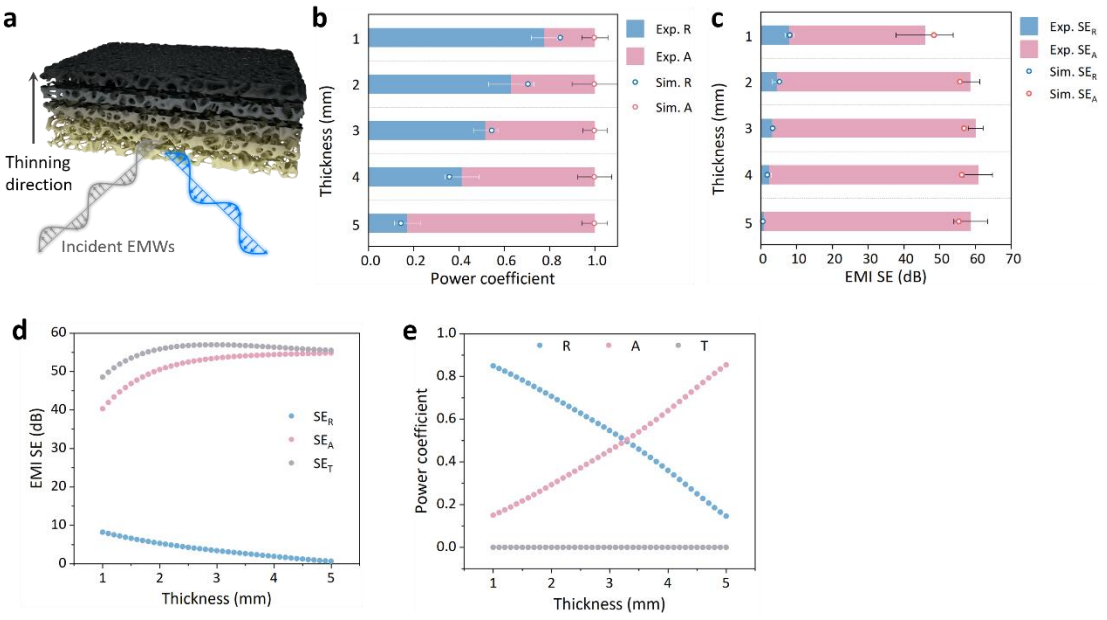

123

124 **Supplementary Fig. 12** a. The thinning effect is conducted by sequentially cutting slices
125 from the low-σ face. Power coefficients (b) and EMI SE (c) as a function of thickness when
126 EMWs impinge from the low-σ face. The thickness is reduced from the low-σ face of
127 sample MCA-94(4). Columns indicate experimental results; dots denote simulation results.
128 For b and c, bars show the mean of three independently prepared specimens, each measured
129 after sequential thinning, and error bars indicate s.d. (n = 3). The continuous thinning effect
130 of EMI SE (d) and power coefficient (e) by simulation results.

131

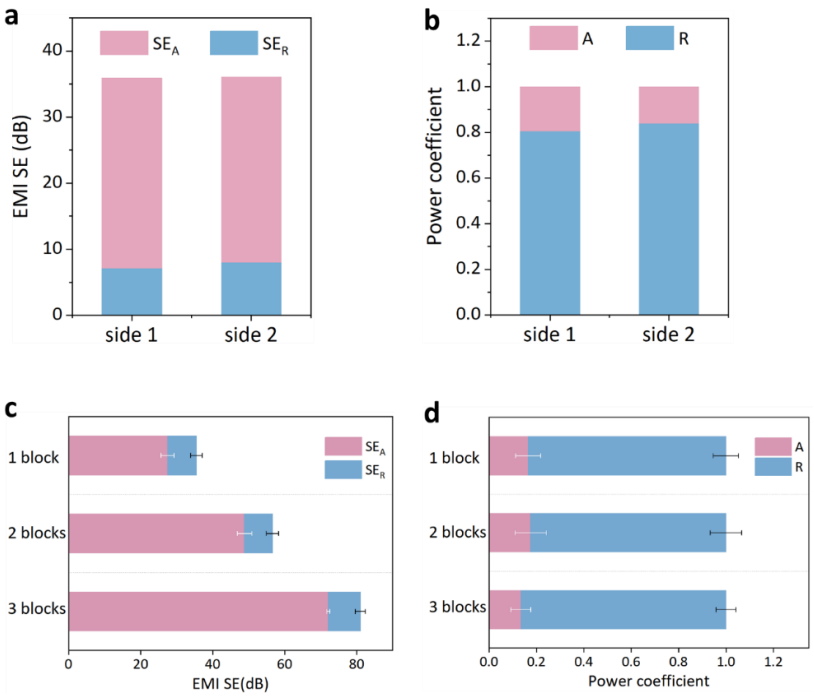

Supplementary Fig. 13 EMI shielding properties of ANF-PVA-PPy (94% porosity) aerogel blocks with uniformly distributed PPy throughout the depth. EMI SE_A, SE_R (a), and power coefficient (b) of a single block when incident from different faces. EMI SE_A, SE_R (c), and power coefficient (d) as a function of different numbers of stacking blocks. For c and d, stacked bars show the mean, and error bars indicate s.d.; n=3 independent specimens.

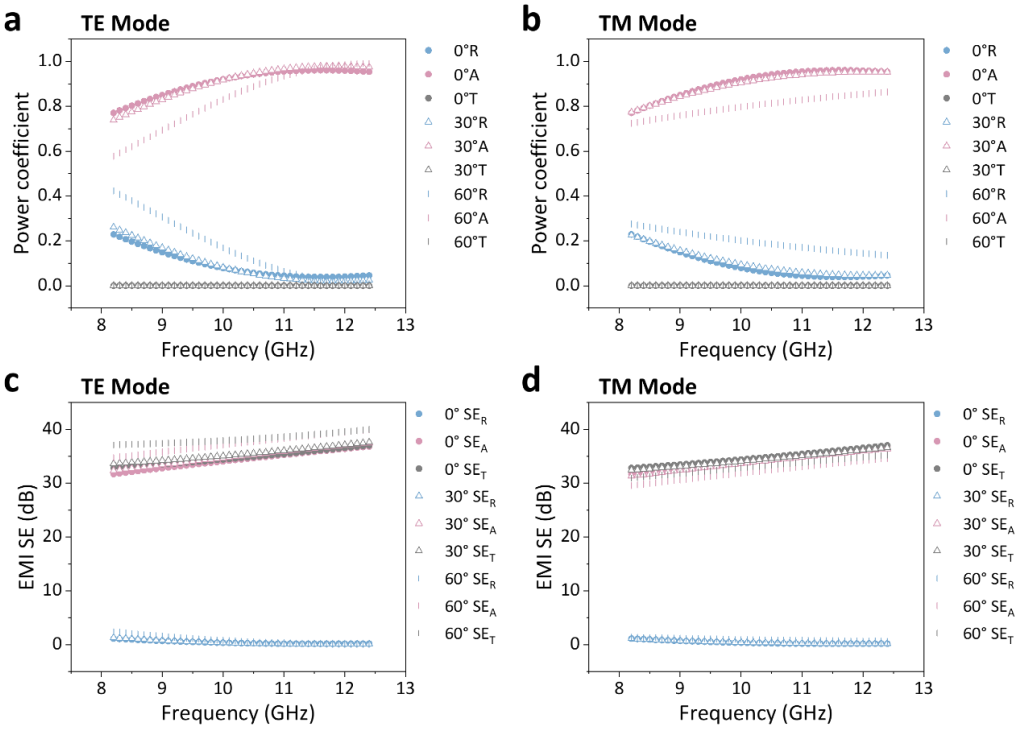

Supplementary Fig. 14 Simulated oblique-incidence EMI shielding response under TE and TM polarizations. Frequency-dependent absorption (*A*), reflection (*R*), and transmission (*T*) of the gradient shielding material under (a) TE and (b) TM polarizations, together with the corresponding shielding-effectiveness components, including reflection shielding effectiveness (SE_R), absorption shielding effectiveness (SE_A), and total shielding effectiveness (SE_T), under (c) TE and (d) TM polarizations. The data are shown at incident angles of 0°, 30°, and 60° over 8.2–12.4 GHz.

To evaluate the shielding robustness beyond the waveguide configuration, we performed full-wave simulations under oblique incidence at 0°, 30°, and 60° for both TE and TM polarizations. The frequency-dependent *A*, *R*, and *T* responses remain stable over 8.2–12.4 GHz. In all cases, *T* is strongly suppressed and remains negligible ($T < 0.08\%$), indicating that the incident electromagnetic waves are effectively attenuated within the gradient shielding material. Although the relative proportions of absorption and reflection vary with incident angle and polarization, absorption consistently dominates over reflection ($A > R$), confirming the absorption-dominated shielding mechanism. This trend is further supported by the corresponding shielding-effectiveness analysis, where the total shielding effectiveness (SE_T) is mainly contributed by absorption shielding effectiveness (SE_A), while reflection shielding effectiveness (SE_R) remains comparatively small. These results demonstrate that the gradient architecture maintains robust broadband EMI shielding under oblique incidence and different polarization states, highlighting its effectiveness in practical electromagnetic environments beyond the ideal waveguide configuration.

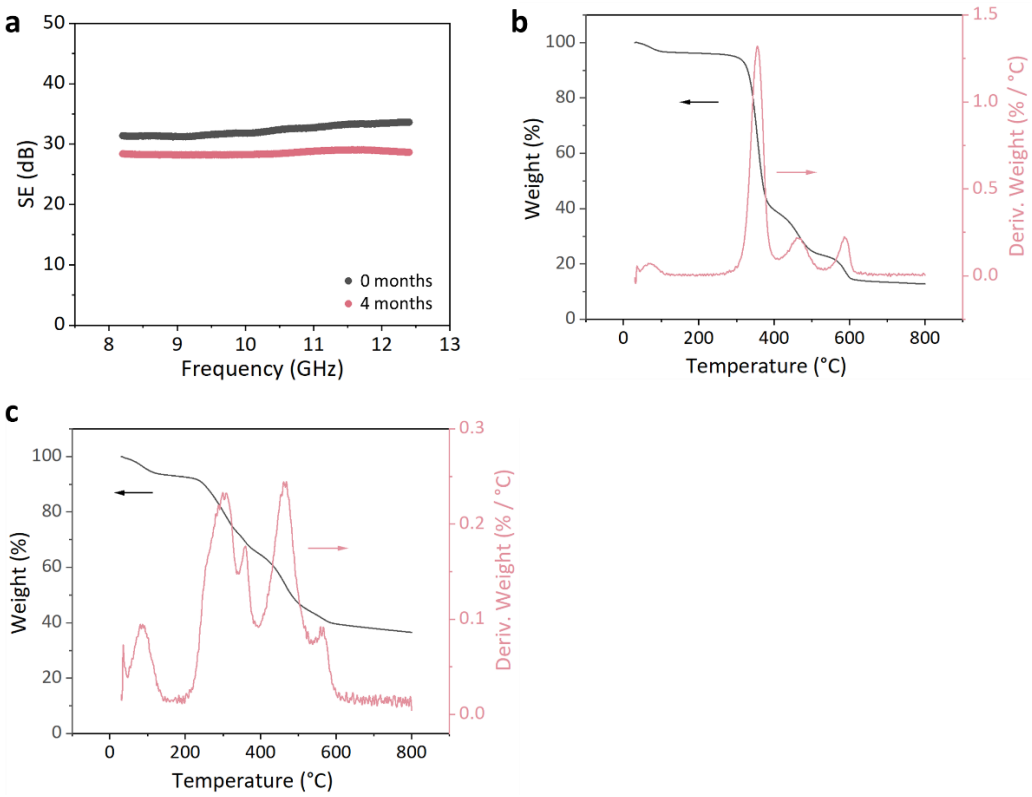

Supplementary Fig. 15 MCAs stability. a. EMI *SE* of MCAs tested in 0 month and in 4 months after formation. Thermogravimetric analysis (TGA) of the prepared samples of 94% porosity ANF-PVA aerogel (b) and the PPy integrated MCA-94 (c).

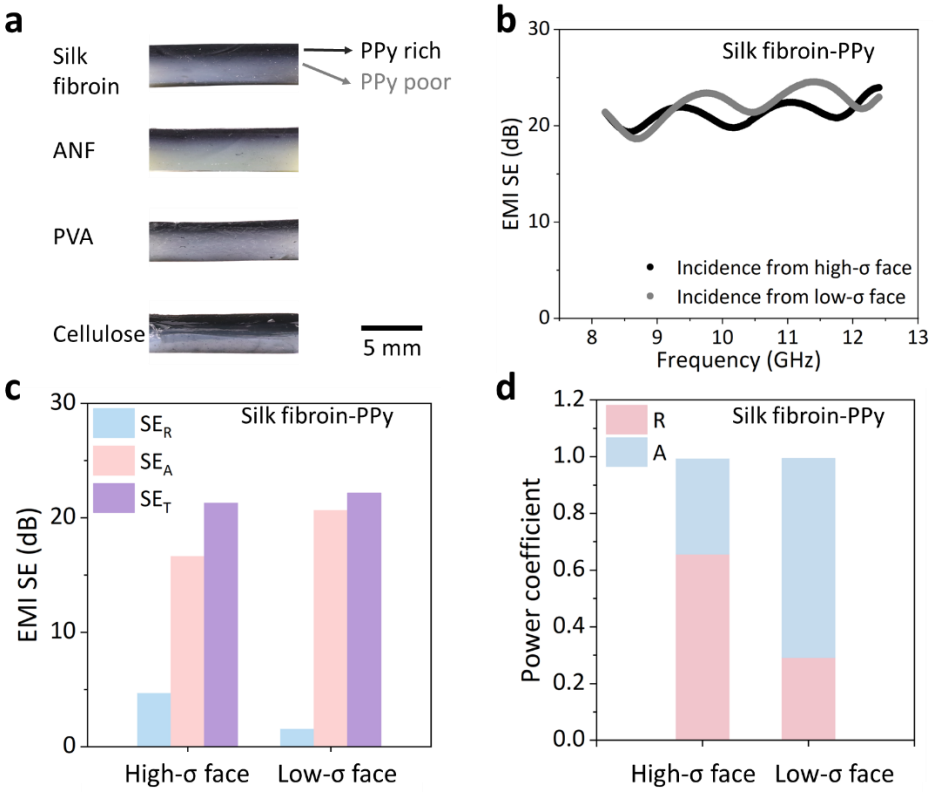

Supplementary Fig. 16 Scaffold-level compatibility of PPy gradient formation. a. In situ growth of PPy in different porous scaffolds, including silk fibroin, ANF, PVA, and bacterial-cellulose hydrogel, forming visible PPy gradients. b-d, EMI shielding properties of a representative silk fibroin–PPy gradient aerogel: (b) EMI SE across the X band; (c) SE_A, SE_R, and SE_T; and (d) power coefficients for incidence from the low-conductivity and high-conductivity faces.

To probe scaffold-level compatibility, we applied an analogous one-sided Py/$FeCl_3$ reaction–diffusion process to chemically distinct wettable porous scaffolds, including silk fibroin, ANF, PVA, and bacterial-cellulose hydrogel. All samples developed visible dark-to-light PPy distributions, consistent with gradient deposition. As a representative non-ANF system, the silk fibroin–PPy gradient aerogel was further evaluated for EMI shielding. The silk fibroin–PPy aerogel exhibited comparable X-band total SE_T under opposite incident directions, but showed direction-dependent shielding contributions: low-σ-face incidence resulted in lower reflection and higher absorption than high-σ-face incidence. These results support the scaffold-level compatibility of the PPy reaction–diffusion route and indicate that the asymmetric absorption-dominated shielding behavior can be retained in a non-ANF scaffold.

For the aqueous PPy system, successful gradient formation requires a wettable, structurally stable porous monolith that allows through-thickness monomer/oxidant transport and retains nascent PPy before complete precursor homogenization. The effective

gradient depth can be tuned by diffusion–reaction conditions and scaffold tortuosity, while the monolithic thickness should exceed the targeted gradient length. Larger-area samples should be feasible by scaling the one-sided precursor-delivery and drying setup, with the practical size limited by mold design and supercritical-drying capacity.

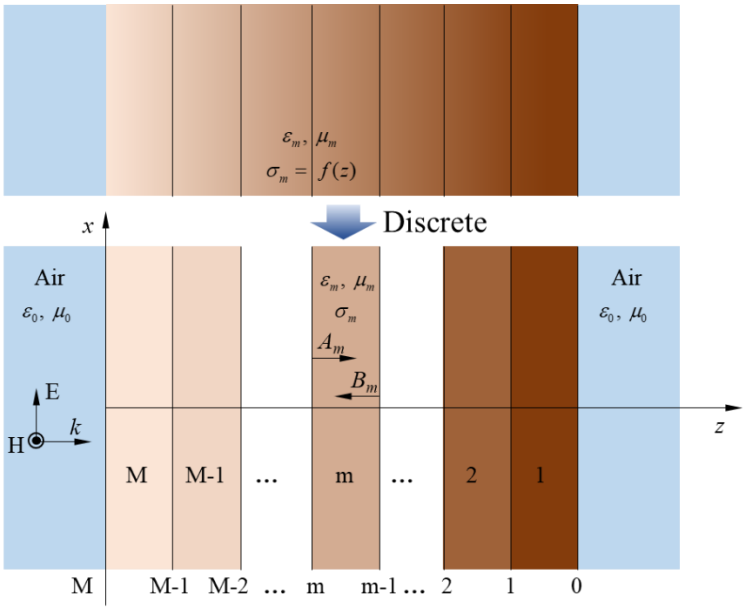

Supplementary Fig. 17 Schematic of electromagnetic wave propagation in a multilayer structure.

Modeling assumptions of the GSM. The present GSM is a reduced-order effective-medium model rather than a full layer-resolved constitutive reconstruction. In the calculations, each stratum is treated as a homogeneous and isotropic effective layer, μ_r is taken as ~1, ε_r* is treated as a constant background dielectric response with $\varepsilon' = 3.5$ and $\tan\delta = 0.07$, and σ is described by the experimentally fitted, frequency-independent profile $\sigma(z) = \sigma_0 \exp(-z/\lambda)$. Porosity and PPy-network connectivity are not introduced as independent variables, but are implicitly included in the effective parameters, including permittivity and σ(z). These assumptions isolate the first-order role of the conductivity gradient and capture the main X-band/10 GHz mechanism, including orientation-dependent S-parameters and field/loss redistribution. However, the approximation may become less accurate toward the Ka band or in highly conductive internal regions, where interfacial polarization, hopping/tunneling transport, and depth-dependent $\varepsilon^*(z,f)$ and $\sigma(z,f)$ dispersion may become important. In such cases, a coupled $\varepsilon^*(z,f)$–$\sigma(z,f)$–porosity/connectivity model would be required for quantitative layer-by-layer prediction.

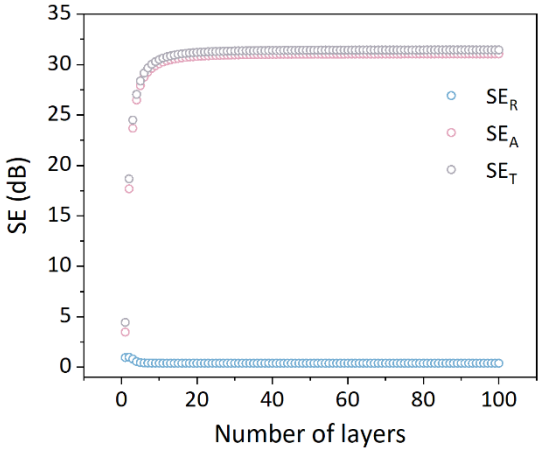

Supplementary Fig. 18 The continuous conductivity profile $\sigma=\sigma_0 \exp(-z/\lambda)$ was discretized into N uniform layers. EMI SE versus the number of gradient layers under incidence from the low-σ face, showing that increasing gradient continuity reduces reflection, increases absorption, and enhances total SE.

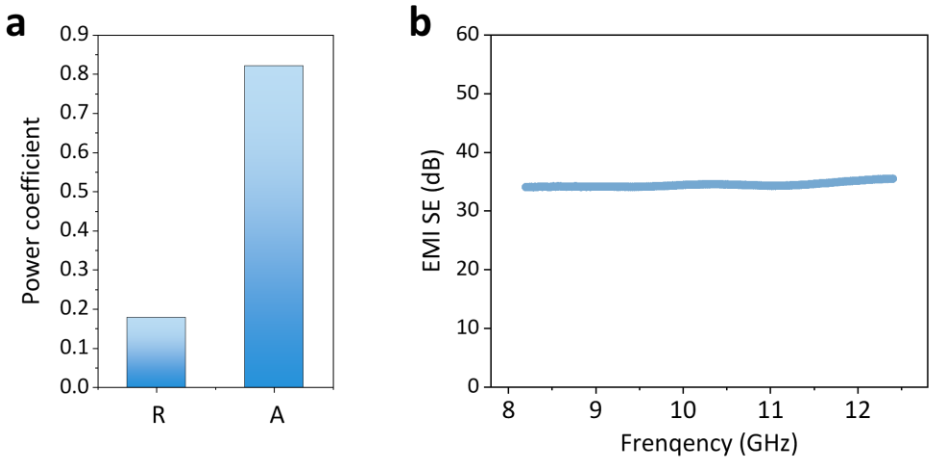

Supplementary Fig. 19 EMI shielding performance of a 3-layer stepwise conductivity-gradient control using the same ANF-PVA/PPy material system. a. Power coefficients *R* and *A* of the 3-layer stepwise conductivity-gradient control under incidence from the low-σ face (transmission is negligible). b. EMI shielding effectiveness (SE) of the same sample across the X band (8.2–12.4 GHz). The 3-layer stepwise control approximates the continuous conductivity profile with three discrete conductivity levels and exhibits effective shielding (SE_T ~ 34 dB) together with absorption-dominant behavior (*R* ~ 0.18, *A* ~ 0.82), while still showing higher reflection than the monolithic continuous-gradient MCA-4*.

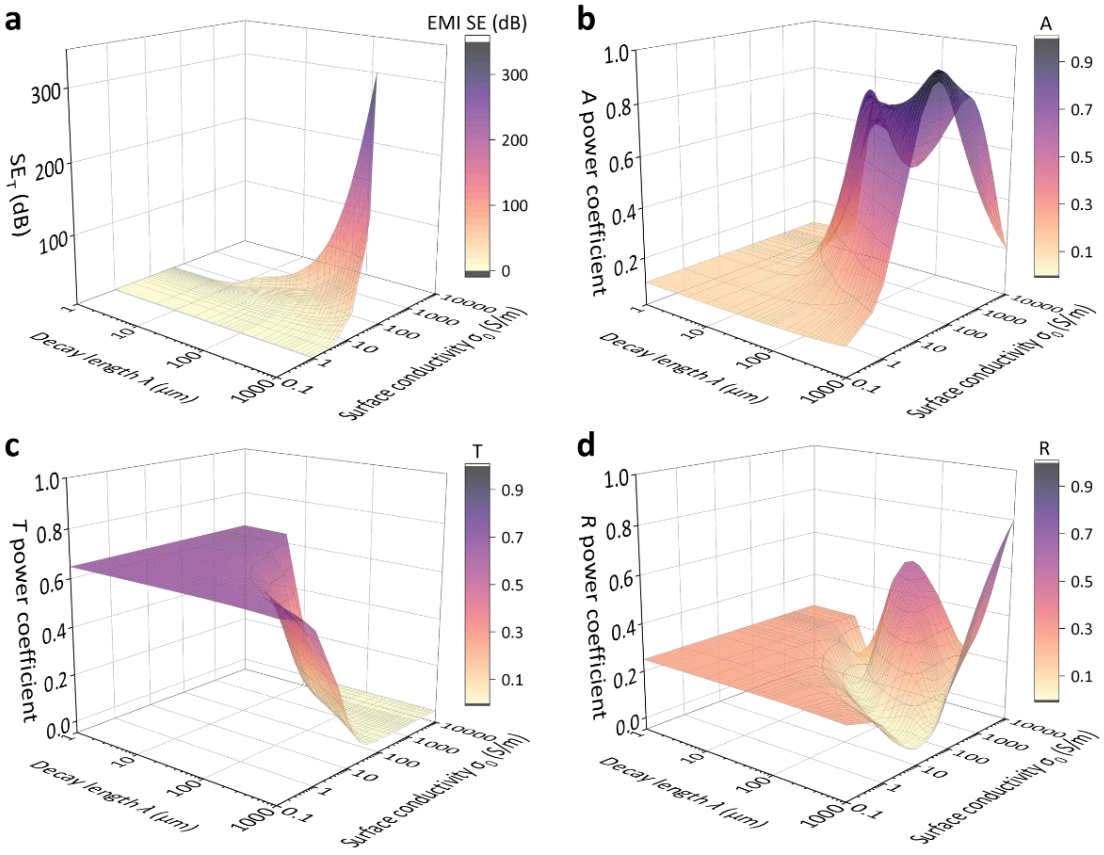

Supplementary Fig. 20 Simulation-derived design maps for conductivity-gradient shields. 3D surface plots showing the dependence of (a) total shielding effectiveness SE_T, (b) absorption power coefficient A, (c) transmission power coefficient T, and (d) reflection power coefficient R on surface conductivity σ_0 and gradient decay length λ for an exponential conductivity profile $\sigma(z) = \sigma_0 \exp(-z/\lambda)$. Simulations were conducted at d = 5 mm and an incident EMW frequency of 10 GHz under low-σ-face incidence.

The maps reveal three design regimes. First, low σ_0 and/or overly small λ gives insufficient distributed loss, resulting in high T and inadequate SE_T. Second, excessive σ_0 or overly large λ suppresses T but increases incident-side σ, reintroducing entrance-side impedance mismatch thereby increasing R. Third, an intermediate σ_0–λ window simultaneously suppresses T and R, producing high absorption. Because $A = 1 - R - T$, a SE_T target > 30 dB corresponds to $T \leq 10^{-3}$; therefore, within the low-T regime, the target $R \leq 0.1$ is essentially equivalent to $A \geq 0.899$, i.e., $A > 0.9$. In summary, the maps indicate that the optimal region of high SE_T ($\geq$ 30 dB) with low-R ($\leq$ 0.1)/high-A (> 0.9) occurs only at intermediate σ_0 and λ, where entrance-impedance matching and internal maximum dissipation are simultaneously satisfied.

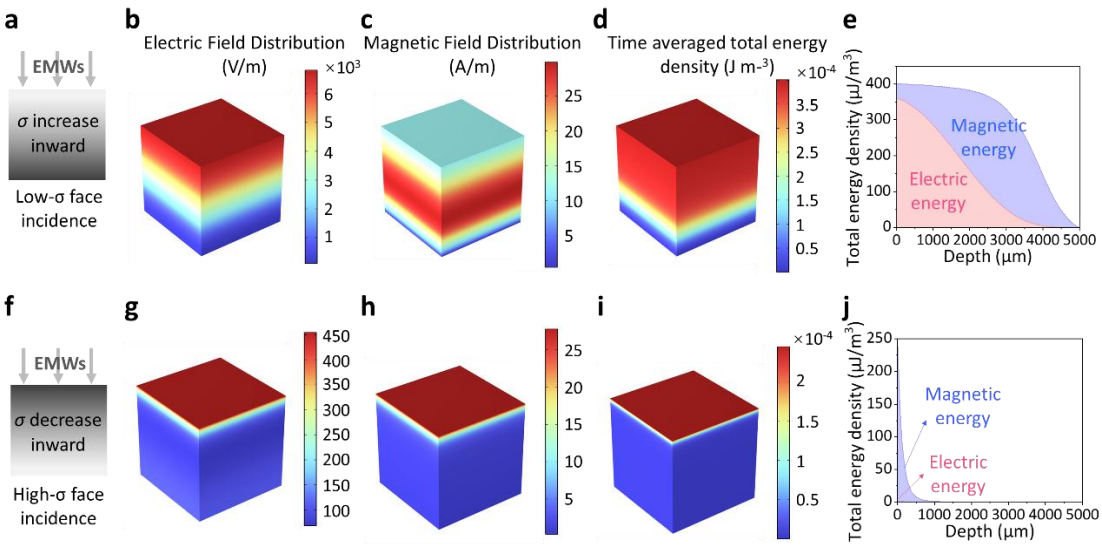

Supplementary Fig. 21 Simulated field, energy-density, and energy-partition distributions for opposite incidence directions in a representative conductivity-gradient MCA at 10 GHz. (a–e) Illustration and simulation results for low-σ face incidence. a, Schematic showing electromagnetic waves incident from the low-σ face, where conductivity increases toward the interior. b–d, Three-dimensional distributions of electric-field magnitude $|\mathbf{E}|$(b), magnetic-field magnitude $|\mathbf{H}|$(c), and time-averaged total electromagnetic energy density (d). e, Corresponding depth-dependent decomposition of total electromagnetic energy into electric and magnetic contributions. (f–j) Illustration and simulation results for high-σ face incidence. f, Schematic showing incidence from the high-σ surface, where conductivity decreases toward the interior. g–i, Three-dimensional distributions of $|\mathbf{E}|$(g), $|\mathbf{H}|$(h), and total electromagnetic energy density (i). j, Corresponding depth-dependent decomposition of total electromagnetic energy into electric and magnetic contributions.

For low-σ face incidence, $|\mathbf{E}|$and the total electromagnetic energy density decay gradually through the aerogel, with the energy density decreasing from 4.01×10^{-4} to 1.29×10^{-7} J m^{-3} over 5 mm, corresponding to 34.9 dB attenuation and consistent with the experimentally measured SE_T. The attenuation is slow over the first ~3000 μm and then accelerates as the wave reaches more conductive regions and accumulates dielectric and ohmic losses. By contrast, under high-σ face incidence, the field and energy density collapse near the entrance, with the energy density reaching its 1/*e* value within ~150 μm, consistent with strong entrance-side mismatch and near-surface field confinement. These results support a direction-dependent mechanism in which low-σ face incidence enables progressive impedance matching and absorption-dominated attenuation, whereas high-σ face incidence produces stronger front-surface reflection.

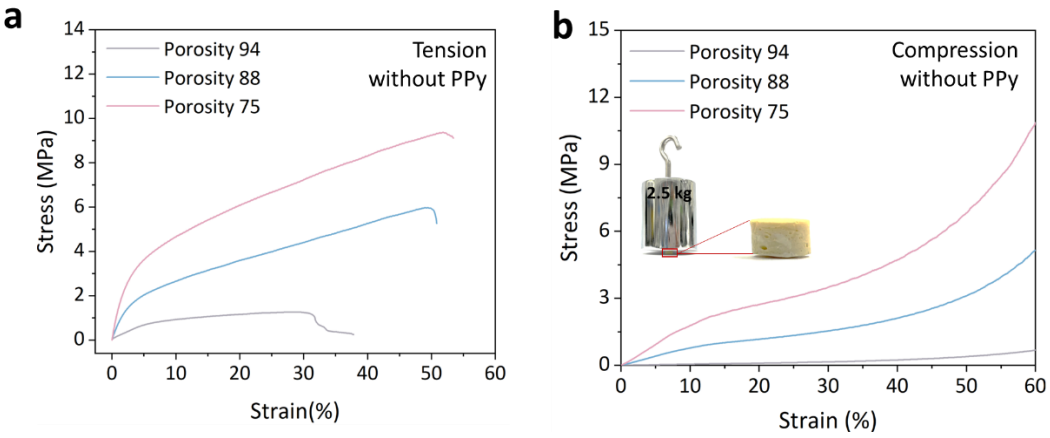

Supplementary Fig. 22 Effects of porosity on the mechanical properties of the pure ANF-PVA aerogel substrates. The tensile (a) and compression (b) responses of aerogels with varied porosities of ANF-PVA aerogel.

Porosity-mediated electromechanical trade-off in MCAs. In the 4 h, ~5 mm porosity-tuned MCA series, decreasing porosity increases diffusion tortuosity and restricts PPy penetration, thereby shortening the conductive-gradient transition and reducing λ. The 94% porosity sample prepared for 4 h, MCA-4/MCA-94, has σ_0 of 900 S m^{-1} and λ of 450 μm, giving SE_T of 49.5 dB, R of 0.16, and A of 0.84. By contrast, MCA-75 has σ_0 of 1100 S m^{-1} and λ of 325 μm, giving higher SE_T of 59.5 dB but larger R of 0.33 and lower A of 0.67. Thus, densification enhances transmission blocking but makes the conductivity transition steeper, weakens progressive impedance matching, and shifts the response from absorption toward reflection in the present processing window. Noted that it is not a universal consequence of densification itself, but a result of the σ_0–λ pair moving away from the GSM-defined high-absorption/low-reflection window. Mechanically, however, the denser nanofibrillar network improves load bearing. The Young's modulus and tensile strength increase from 26 MPa and 1.27 MPa for MCA-94 to 205 MPa and 12.12 MPa for MCA-75. Therefore, MCA-4* represents the broadband low-reflection/high-absorption optimum, whereas MCA-75 prioritizes mechanical robustness and shielding effectiveness.

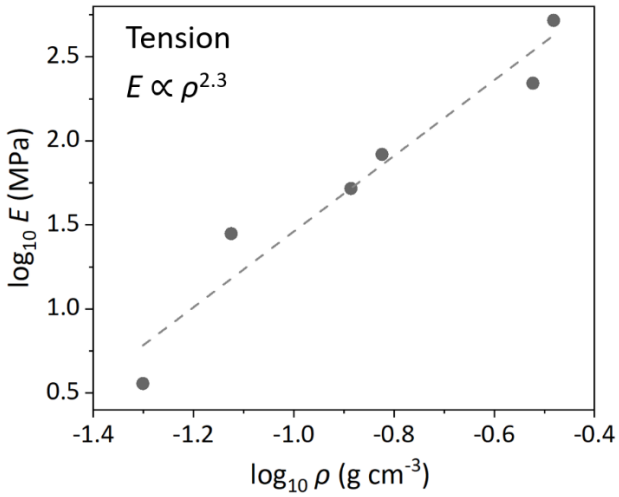

Supplementary Fig. 23 Tensile modulus of MCAs plotted against their densities, derived from experimental data (dots) and theoretical fitting (dashed lines). This function exhibits the typical power-law dependence observed in aerogel materials. This trend aligns with the behavior observed under tensile loading.

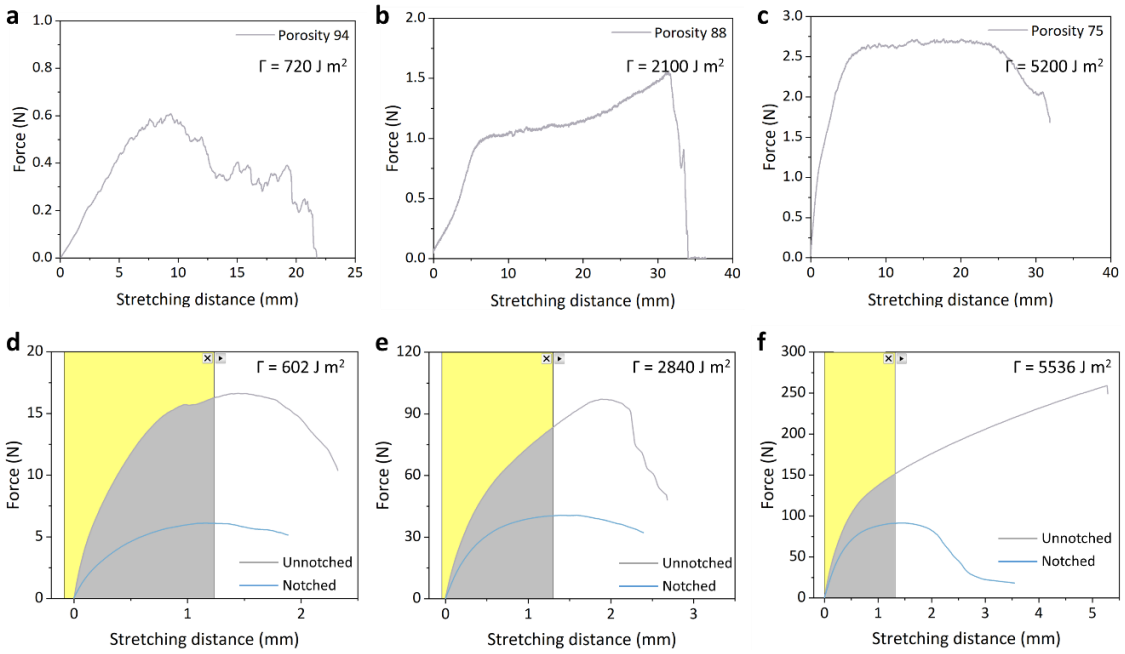

298

299 **Supplementary Fig. 24** Fracture energies of MCAs characterized by tearing tests (a-c) and
300 pure shear tests (d-f). Force-displacement curves of tearing test and the calculated tearing
301 energies for MCA-94 (a), MCA-88 (b), and MCA-75 (c). Force-displacement curves of
302 pure shear test for unnotched and notched samples, and the calculated fracture energies for
303 MCA-94 (d), MCA-88 (e), and MCA-75 (f).

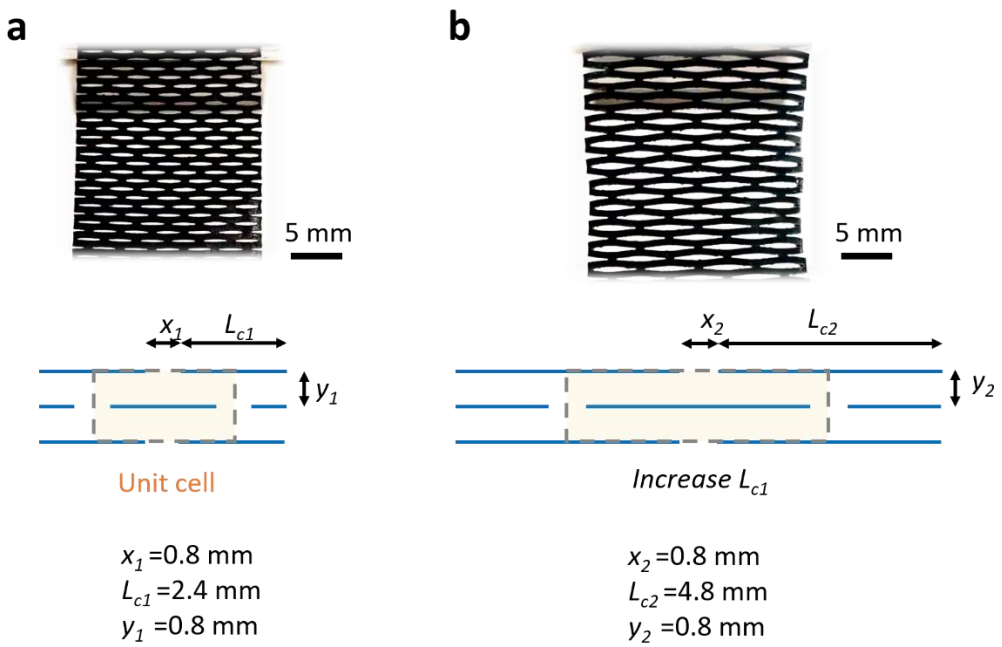

Supplementary Fig. 25 MCA Kirigami with periodic laser-cut slits. a. Digital images of the kirigami pattern (upper panel) and cut-pattern unit cell (lower panel) marked in the yellow box. Cuts are indicated by the blue horizontal lines. b. Digital images (upper panel) and corresponding cut-pattern unit-cell schematic (lower panel) of the kirigami specimen with increased L_c. L_c indicates the length of the cut, x indicates the spacing in the transverse direction, and y indicates the spacing in the axial direction. Scale bars, 5 mm.

Periodic straight-line patterns created by laser cutting were designed with cut length L_c below one-quarter of the free-space wavelength at the upper band edge (f = 12.4 GHz, $\lambda_0/4 = 6.04$ mm) of the X-band measurement. This conservative rule keeps the slits well below the first slot/aperture resonance scale ($\sim \lambda_0/2$) and thereby limits aperture-induced scattering/transmission while preserving shielding performance.

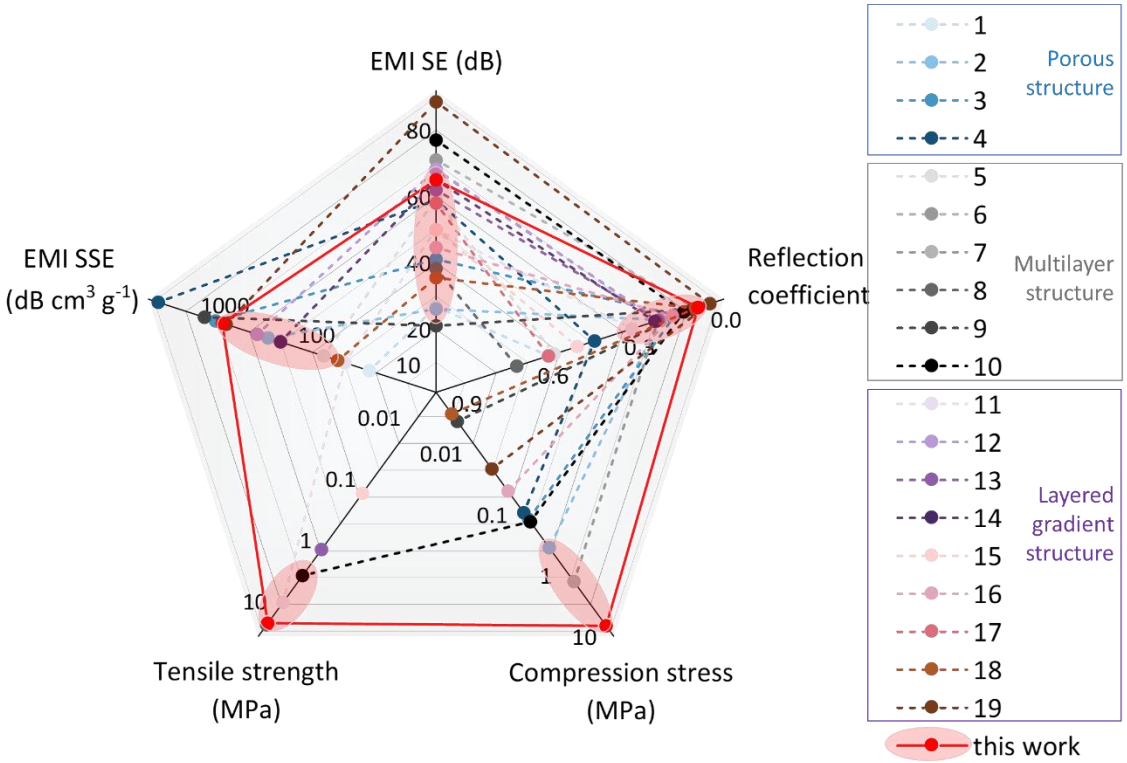

316

317 **Supplementary Fig. 26** Radar plot of MCAs compared with other porous EMI shielding
318 materials with low reflectivity. The performance of the recently reported absorption-
319 dominated EMI SE materials is summarized in Table 2.

320

Supplementary Table 1 Design table of conductivity gradient parameters and EMI shielding performance of key MCA specimens.

Specimen	Porosity (%)	Thickness (mm)	σ_0 (S/m)	λ (μm)	R^2	X band			Ka band		
						SE_T (dB)	*R*	*A*	SE_T (dB)	*R*	*A*
MCA-1	94	5	900	225	0.84	42.2	0.24	0.76	—	—	—
MCA-2	94	5	900	340	0.78	46.7	0.19	0.82	—	—	—
MCA-4	94	5	900	450	0.98	49.5	0.16	0.84	—	—	—
MCA-6	94	5	900	485	0.91	52.5	0.22	0.78	—	—	—
MCA-88	88	5	950	380	0.92	54.0	0.28	0.72	—	—	—
MCA-75	75	5	1100	325	0.99	59.5	0.33	0.67	—	—	—
MCA-4*	94	5	350	450	0.94	32.3	0.09	0.91	41.9	0.08	0.92

Note: Values are band-averaged under low-σ-face incidence. X-band: 8.2–12.4 GHz; Ka-band: 26.5–40.0 GHz. R^2 denotes the coefficient of determination for the exponential-profile fit. MCA-4/MCA-94 denotes the 94% porosity sample prepared with a 4 h diffusion/reaction time. MCA-4* denotes the intentionally reduced-surface-conductivity sample derived from MCA-4. "—", not determined; Ka-band data were collected only for the optimized MCA-4* sample used for broadband validation; they were not measured for the X-band screening specimens.

Supplementary Table 2 Mechanical performance of MCAs.

Sample	Young's modulus (MPa)	Tensile stress (MPa)	Elongation at fracture (%)	Toughness ($J\ m^{-3}$)	Fracture energy ($J\ m^{-2}$)	Compression stress @60% (MPa)
MCA-94	26	1.27	34.9	3.16×10^{5}	602	0.69
MCA-88	80	4.77	40.79	1.48×10^{6}	2840	5.51
MCA-75	205	12.12	50.55	4.29×10^{6}	5536	13.26

Supplementary Table 3 Comprehensive performance of recent absorption-dominated EMI shielding materials.

No.	SE (dB)	*R* coefficient	*A* coefficient	Band (GHz)	Bandwidth (A> 0.9)	Compress-ion stress (MPa) at specific strain	Tensile strength (MPa)	SSE (dB $cm^3 g^{-1}$)	SSE/t (dB $cm^2 g^{-1}$)	SE/t (dB cm^{-1})	Thic-kness (mm)	Density (g/cm^3)	Stru-cture	Re-ference
1	26.8	0.61	0.39	8.2-12.4	0	—	—	26.8	127.62	134	2	1	porous	4
2	26.1	0.224	0.78	8.2-12.4	0	0.70 (70%)	—	342.7	1373-1518	104.4	2.5	0.076	porous	5
3	41.1	0.17	0.83	8.2-12.4	0	0.361 (80%)	—	1280	6400	205.5	2	0.032	porous	6
4	59	0.45	0.55	8.2-12.4	0	0.00187 (70%)	—	5420.5	10841	118	5	0.01	porous	7
5	21	0.11	0.89	18-26.5	0	0.006 (40%)	—	1690	3370	42	5	0.014	porous	8
6	59.4	0.59	0.41	8.2-12.4	0	—	—	84.5	422.5	297	2	0.723	multilayer	9
7	71	0.1	0.9	8.2-12.4	2.5	—	—	—	—	273.1	~2.6	—	multilayer	10
8	68	0.23	0.77	8.2-12.4	0	2.5 (60%)	—	—	—	123.6	5.5	—	multilayer	11
9	38.3	0.72	0.28	8.2-12.4	0	—	12.8	—	—	212.8	1.8	—	multilayer	12
10	77	0.14	0.86	8.2-18	0	0.264 (50%)	2	—	—	385	2	—	multilayer	13
11	50	0.32	0.68	8.2-12.4	0	—	5.5	49.6	12390	12500	0.04	1	gradient	14
12	68.2	0.23	0.77	8.2-12.4	0	—	—	448.7	897.4	136.4	5	0.152	gradient	15
13	62	0.23	0.77	8.2-12.4	0	—	0.75	—	—	310	2	—	gradient	16
14	65	0.24	0.76	8.2-12.4	0	—	—	250	500	130	5	0.26	gradient	17
15	50.0	0.51	0.49	8.2-12.4	0	—	0.07	—	—	2777.8	0.18	—	gradient	18
16	44.6	0.18	0.82	8.2-12.4	0	0.0833 (80%)	—	—	—	148.7	3	—	gradient	19
17	58	0.61	0.39	8.2-12.4	0	—	—	—	—	1705.9	0.34	—	gradient	20
18	35.5	0.085	0.915	8.2-12.4	0	4.5 (70%)	—	86.7	144.5	59.2	6	0.409	gradient	21

19	88.5	0.05	0.95	8.2-12.4	3.5	0.036 (50%)	—	983.3	2892.1	260.3	3.4	0.09	gradient	22
20	20-65	0.09-0.4	0.9	8.2-40	29.8	0.7-13.3 (60%)	1.3-12.1	67-1083	134-2166	60-600	~5	0.06-0.3	Continuous gradient	This work

Note: Bandwidth is defined as the continuous frequency window over which $A > 0.9$, unless otherwise specified in the original reference. "—" denotes not determined.

References

1 Sakthivel, S. & Boopathi, A. Synthesis and characterization of polypyrrole (PPy) thin film by spin coating Technique. *J. Chem. Chem. Sci* **4**, 150-155 (2014).

2 Zhu, J. et al. Branched Aramid Nanofibers. *Angew. Chem. Int. Ed.* **56**, 11744-11748 (2017).

3 Tan, Y. & Ghandi, K. Kinetics and mechanism of pyrrole chemical polymerization. *Synth. Met.* **175**, 183-191 (2013).

4 Zhang, H. et al. Multifunctional microcellular PVDF/Ni-chains composite foams with enhanced electromagnetic interference shielding and superior thermal insulation performance. *Chem. Eng. J.* **379**, 122304 (2020).

5 Yu, Z., Dai, T., Yuan, S., Zou, H. & Liu, P. Electromagnetic interference shielding performance of anisotropic polyimide/graphene composite aerogels. *ACS Appl. Mater. Interfaces* **12**, 30990-31001 (2020).

6 Wang, Y.-Y. et al. Lightweight and robust carbon nanotube/polyimide foam for efficient and heat-resistant electromagnetic interference shielding and microwave absorption. *ACS Appl. Mater. Interfaces* **12**, 8704-8712 (2020).

7 Yang, G.-Y. et al. Ultralight, Conductive Ti3C2Tx MXene/PEDOT:PSS Hybrid Aerogels for Electromagnetic Interference Shielding Dominated by the Absorption Mechanism. *ACS Appl. Mater. Interfaces* **13**, 57521-57531 (2021).

8 Pitkänen, O. et al. Lightweight Hierarchical Carbon Nanocomposites with Highly Efficient and Tunable Electromagnetic Interference Shielding Properties. *ACS Appl. Mater. Interfaces* **11**, 19331-19338 (2019).

9 Yang, J. et al. Gradient structure design of lightweight and flexible silicone rubber nanocomposite foam for efficient electromagnetic interference shielding. *Chem. Eng. J.* **390**, 124589 (2020).

10 Liu, A. et al. Asymmetric Structural MXene/PBO Aerogels for High-Performance Electromagnetic Interference Shielding with Ultra-Low Reflection. *Adv. Mater.*, 2414085 (2024).

11 Yang, J., Wang, H., Zhang, Y., Zhang, H. & Gu, J. Layered Structural PBAT Composite Foams for Efficient Electromagnetic Interference Shielding. *Nanomicro Lett.* **16**, 31 (2023).

12 Xue, B. et al. Directional electromagnetic interference shielding based on step-wise asymmetric conductive networks. *Nanomicro Lett.* **14**, 1-16 (2022).

13 Hu, X. et al. Multifunctional Flexible WPU Composite Aerogels with Sandwich Structure for Dual-Sided Low-Reflection Electromagnetic Interference Shielding. *Adv. Funct. Mater.* e17665 (2025).

14 Lee, S., Nguyen, N. K., Kim, M., Park, P. & Nah, J. Conductivity-Controlled Polyvinylidene Fluoride Nanofiber Stack for Absorption-Dominant Electromagnetic Interference Shielding Materials. *ACS Applied Materials & Interfaces* **15**, 33180-33189 (2023).

15 Xue, T. et al. 3D Printed Integrated Gradient-Conductive MXene/CNT/Polyimide Aerogel Frames for Electromagnetic Interference Shielding with Ultra-Low Reflection. *Nano-Micro Letters* **15**, 45 (2023).

16 Xu, Y., Hou, M. & Wang, J. Porous Gradient Composite with Dependable Superhydrophobic Protection for Multifunctional Electromagnetic Interference Shielding. *ACS Applied Materials & Interfaces* **16**, 3978-3990 (2024).

17 Lee, S. et al. 3D-printed gradient conductivity and porosity structure for enhanced absorption-dominant electromagnetic interference shielding. *Carbon* **231**, 119759.
18 Zhang, H. et al. Electric-magnetic dual-gradient structure design of thin MXene/Fe3O4 films for absorption-dominated electromagnetic interference shielding. *Journal of Colloid and Interface Science* **678**, 950-958 (2025).
19 Feng, Y. et al. Customizable gradient MXene/polyurethane modules for electromagnetic interference shielding with low reflection and thermal management. *Chemical Engineering Journal* **499**, 155959 (2024).
20 Ma, M. et al. Cellulose nanofiber/MXene/FeCo composites with gradient structure for highly absorbed electromagnetic interference shielding. *Chemical Engineering Journal* **452**, 139471 (2023).
21 Li, Z. et al. Compressible thermoplastic polyurethane/silver nanorod foams for absorption dominant electromagnetic interference shielding. *Journal of Materials Science & Technology* **197**, 9-16 (2024).
22 Lei, Z. et al. Electrically conductive gradient structure design of thermoplastic polyurethane composite foams for efficient electromagnetic interference shielding and ultra-low microwave reflectivity. *Chemical Engineering Journal* **424**, (2021).